A micromagnetic investigation of magnetite grains in the form of Platonic polyhedra with surface roughness

Geochemistry Geophysics Geosystems G3

Article
Volume 12, Number 10
15 October 2011
Q10Z31, doi:10.1029/2011GC003560
ISSN: 1525-2027

Published by AGU and the Geochemical Society

A micromagnetic investigation of magnetite grains in the form of Platonic polyhedra with surface roughness

W. Williams
School of Geosciences, University of Edinburgh, King's Buildings, West Mains Road, Edinburgh, EH9 3JW, UK (Wyn.Williams@ed.ac.uk)

A. R. Muxworthy
Department of Earth Science and Engineering, Imperial College London, South Kensington Campus, London, SW7 2AZ, UK

M. E. Evans
Institute for Geophysical Research, University of Alberta, Edmonton, Alberta, T6G 2G7, Canada

[1] Micromagnetic calculations have been carried out for spherical magnetite particles with surface roughness consisting of patterns of conical bumps based on regular (Platonic) convex polyhedra. The purpose was to examine the effect of surface irregularities while avoiding overall shape anisotropy, which generally plays a dominant role in determining hysteresis properties. We considered three morphologies based on the tetrahedron (4 apices), the icosahedron (12 apices), and the dodecahedron (20 apices). Grains of three sizes were considered: 30 nm (single-domain, SD), 90 nm (on the single-domain/pseudo-single-domain boundary, SD/PSD), and 120 nm (stable pseudo-single-domain, PSD). We find that the morphologies investigated have very little effect on the hysteresis parameters of SD and marginal SD/PSD grains. However, in the PSD grains, coercivity increases significantly as bump amplitude increases from 0.1 to 0.9. This lends support to the long-standing notion that surface protuberances on larger grains are a possible source of paleomagnetically significant stable remanence, although the very high coercivities (on the order of 100 mT) observed in some rocks cannot be achieved. Classical Stoner-Wohlfarth shape anisotropy remains the only explanation for such ultra-stable remanence in magnetite-bearing rocks. This is confirmed by a specific example of a model "skeletal" grain consisting of three orthogonal parallelepipeds.

Components: 4100 words, 10 figures, 1 table.

Keywords: magnetite; micromagnetism; modeling.

Index Terms: 1518 Geomagnetism and Paleomagnetism: Magnetic fabrics and anisotropy; 1540 Geomagnetism and Paleomagnetism: Rock and mineral magnetism.

Received 1 May 2011; **Revised** 25 August 2011; **Accepted** 9 September 2011; **Published** 15 October 2011.

Williams, W., A. R. Muxworthy, and M. E. Evans (2011), A micromagnetic investigation of magnetite grains in the form of Platonic polyhedra with surface roughness, *Geochem. Geophys. Geosyst.*, *12*, Q10Z31, doi:10.1029/2011GC003560.

Theme: Magnetism From Atomic to Planetary Scales: Physical Principles and Interdisciplinary Applications in Geoscience

1. Introduction

[2] In a recent paper [*Williams et al.*, 2010], we reported results from a series of micromagnetic calculations aimed at assessing the role of irregular morphology on the magnetic properties of magnetite grains in rocks. Those calculations were motivated by a much earlier suggestion by *Stacey* [1961, p. 1256] that "small irregular protuberances" on larger grains might be the source of stable remanence in paleomagnetic samples. The results, however, did not support this idea. For the most part, surface bumps had little effect on—or even lowered—the coercivity, except where grains carried a small number of large bumps that endow the grain with overall shape anisotropy. For example, 30 nm particles carrying many bumps (characterized by small angular separation, $\theta = 5°$) showed a decrease in coercivity by a factor of two as the relative bump size (R, the ratio of bump amplitude to particle radius) varied from 0.1 to 0.9. The surface irregularities act as nucleation centers for micromagnetic changes, thereby lowering the coercivity. On the other hand, the overall shape anisotropy of models with fewer bumps ($\theta = 90°$) caused the coercivity to increase by a factor of two over the same range of R [see *Williams et al.*, 2010, Figure 3a].

[3] The primary goal of the present work was to investigate the influence of surface irregularities on magnetic behavior without introducing overall shape anisotropy. To this end, we report here a series of micromagnetic calculations based on three of the regular (Platonic) polyhedra: the tetrahedron (with four apices), the icosahedron (with twelve), and the dodecahedron (with twenty). To place these simulations in their full context, we carried out two other sets of calculations. A preliminary set considers the micromagnetic behavior of grains carrying a single conical bump. The effects of shape anisotropy cannot be excluded in such a model, but the calculations are nevertheless useful because they enable one to explore the distortion in micromagnetic structure—and its effects on hysteresis—caused by the interplay of the crystallographic orientation of the bump, its amplitude, and the direction of the magnetizing field. In the other set, a high-resolution micromagnetic simulation of a "skeletal" model of the same geometry as that examined by *Tauxe et al.* [2002] was investigated as a possible source of ultra-stable remanence.

2. Methods

[4] The computational scheme closely follows that of our earlier work [*Williams et al.*, 2010], so we give here only a brief outline. The grain surface is first constructed by defining a suitable finite element mesh, and then the magnetic structure of the entire grain is obtained by minimizing the torque on each discretized magnetic moment according to the Landau-Lifshitz-Gilbert equation [*Suess et al.*, 2002]. The room temperature material parameters of magnetite (Fe_3O_4) are used throughout, namely saturation magnetization, $M_s = 4.8 \times 10^5$ A m^{-1}, exchange constant, $A = 1.34 \times 10^{-11}$ J m^{-1}, and magnetocrystalline anisotropy, $K_1 = 1.24 \times 10^4$ J m^{-3}. As before, we consider grains of three volumes: 0.14×10^{-22} m^3, 3.82×10^{-22} m^3 and 9.05×10^{-22} m^3. These volumes correspond to spheres with diameters of 30 nm, 90 nm and 120 nm respectively, and for brevity will be referred to as these diameters. These sizes correspond to SD grains, grains on the SD/PSD boundary, and stable PSD grains respectively. For each size, we started with spherical grains to which were added 4, 12, or 20 conical bumps of gradually increasing size, the relative amplitudes (R) being 0.1, 0.3, 0.5, 0.7, and 0.9 expressed as fractions of the sphere radius. The base radius of each cone was identical for all models and was chosen arbitrarily to be 0.2 of that of the sphere. The percentage fraction of the grain volume residing in the bumps is given in Table 1.

[5] The bumps were placed on the surface of the sphere symmetrically with respect to the ⟨100⟩ set of axes. The finite element meshing of such conical bumps can be problematic but it has been demonstrated by *Rave et al.* [1998] that the effective fields calculated at such sharp corners do not introduce errors provided the mesh size does not exceed the exchange length. Since magnetic domain structure is sensitive to the grain volume, after the bumps were added the grain volume was re-normalized to that of the starting sphere. Examples of the grain morphologies used are given in Figure 1.

[6] For each model we investigated the micromagnetic structure during field cycling and com-

Table 1. Percentage of Grain Volume Residing in the Bumps on the Sphere Surface

Bump Amplitude (*R*)	Number of Bumps on Sphere Surface			
	1	4	12	20
1	0.10	0.41	1.23	2.03
3	0.27	1.08	3.14	4.55
5	0.44	1.73	5.03	8.10
7	0.60	2.38	6.80	10.83
9	0.77	3.00	8.50	13.29

puted the corresponding values of M_{rs}/M_s and H_c by averaging the values obtained from fields aligned along the easy ⟨111⟩, hard ⟨100⟩, and intermediate ⟨110⟩ directions. In this way, a total of 135 micromagnetic models were computed (3 polyhedra × 3 grain sizes × 5 bump amplitudes × 3 field orientations).

3. Results

3.1. Single Bump

[7] Grains of the same three sizes (30, 90, 120 nm) used for the Platonic models were considered, again with bump sizes (R) of 0.1, 0.3, 0.5, 0.7, and 0.9. For each model, four configurations were investigated: (1) bump along the hard ⟨100⟩ axis, field along the easy ⟨111⟩ axis, (2) bump along the hard axis, field along the hard axis, (3) bump along the easy axis, field along the easy axis, and (4) bump along the easy axis, field along the hard axis. The salient features for the 30 nm, R = 0.9 subset are illustrated in Figures 2 and 3 for the bump along the hard and easy axes, respectively. In both figures the magnetic structures at H = 0 (Remanence) and at H = 80 mT (Saturation) appear in the upper and lower panels, respectively. Figure 2a indicates that the grain has a high remanence aligned along the easy direction except for the bump itself where the magnetization deviates slightly toward the hard direction. This pattern is repeated at saturation (Figure 2c), but the deviating magnetization is now restricted to the very tip of the bump. When the field is applied along the hard direction the magnetization is fully saturated parallel to the applied field (Figure 2d), but when the field is removed (Figure 2b) the magnetization relaxes back to the same pattern as seen in Figure 2a. The evolution of the micromagnetic structure—and the role played by the bump as a nucleation center—during field cycling along the hard direction is best appreciated by viewing Animation S1 in the auxiliary material.[1] In Animation S1, it is seen that the magnetization within the bump induces the rotation of the magnetization in the sphere as the field intensity decreases, thereby reducing the coercivity.

[8] Figure 3a shows that the remanent magnetization remains saturated along the easy direction after the application of a saturating field (Figure 3c). When a field of 80 mT is applied along the hard direction the magnetic structure follows the field toward saturation (Figure 3d), although the magnetic moments in the bump itself deviate toward the easy direction. When the field is removed the remanence state relaxes back to saturation along the easy direction (Figure 3b). Changes in the micromagnetic structure can best be appreciated in Animation S2. In Animation S2, the field is aligned along the ⟨100⟩ direction, and the bump is in the easy direction. For this configuration, the magnetization in the bump is the first to rotate out of the applied field direction before switching, and the last to align in the reverse field direction after switching. In this case, however, the effect on the resulting coercivity is minimal.

[9] Values for the ratio of saturation remanence to saturation magnetization (M_{rs}/M_s) and for the coercive force (H_c) of each of these configurations (2 bump orientations (easy, hard); 3 grain sizes (30 nm, 90 nm, 120 nm); 5 bump amplitudes (0.1, 0.3, 0.5, 0.7, 0.9)) are obtained by averaging the values resulting from fields aligned along the easy ⟨111⟩, hard ⟨100⟩, and intermediate ⟨110⟩ directions. The M_{rs}/M_s ratios exhibit a strong trend between grain sizes, but very little variation within each grain size: for the 30 nm grains $0.80 < M_{rs}/M_s < 0.84$, for 90 nm $0.42 < M_{rs}/M_s < 0.50$, and for 120 nm $0.20 < M_{rs}/M_s < 0.22$.

[10] The corresponding variations in coercive force for all 30 models are summarized in Figure 4. Also shown are the data for the corresponding smooth spheres (R = 0) taken from our earlier paper [*Williams et al.*, 2010]. The smallest of these (30 nm) give the highest values (H_c = 13.2 mT) because they are single-domain (SD) and reverse by coherent rotation. The 90 nm grains are magnetically much softer (H_c = 3.8 mT) because they display incoherent rotation during hysteresis by vortex nucleation and propagation [*Enkin and Williams*, 1994; *Williams et al.*, 2006]. At 120 nm, coercivity begins to rise again (H_c = 6.6 mT) because the

[1] Auxiliary materials are available in the HTML. doi:10.1029/2011GC003560.

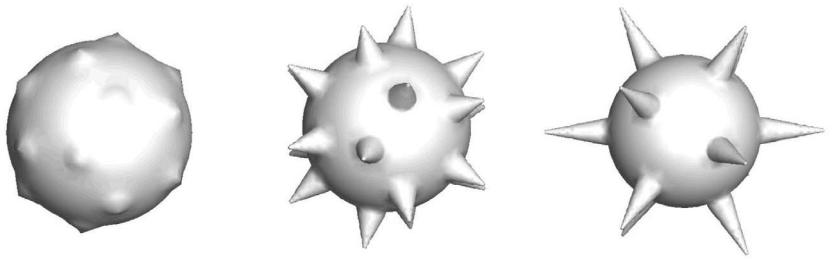

Figure 1. Representative examples of grain morphologies used for the micromagnetic calculations. Conical bumps were places on the surface of a sphere at the vertices of platonic solids: (left) dodecahedron, $R = 0.1$; (middle) dodecahedron, $R = 0.5$; (right) icosahedron, $R = 0.9$. Where R is expressed as a fraction of the radius of the starting sphere.

majority of the remanence is held within the increasingly dominant vortex core. For the larger grain size, the switching mechanism changes from vortex nucleation and propagation to coherent rotation of the vortex, combined with a magnetically softer shell exhibiting incoherent reversal modes.

[11] As bumps are added, very little change occurs prior to R = 0.5. But then significant changes take

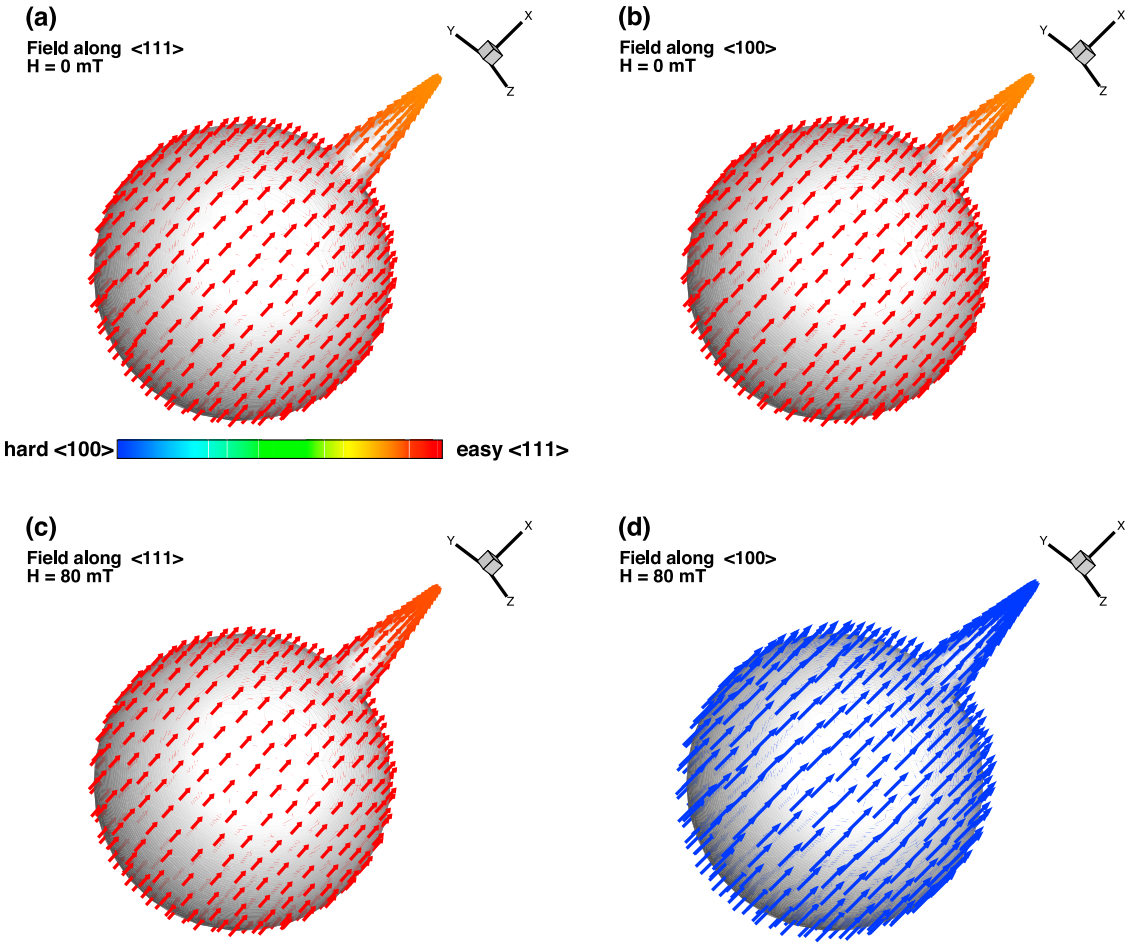

Figure 2. Micromagnetic structure of a 30 nm grain having a single large bump ($R = 0.9$) with its axis parallel to the [100] (hard) axis. (a and b) H = 0 (Remanence); (c and d) H = 80 mT (Saturation). The field direction is indicated in each panel, and the resulting magnetization directions are colored according to the orientation scale bar in Figure 2a. It can be seen that, with the exception of Figure 2d, the easy ⟨111⟩ alignment of the magnetization is slightly perturbed within the bump toward the ⟨100⟩ bump axis. A field of 80 mT is sufficient to saturate the magnetization along the hard ⟨100⟩ direction in Figure 2d.

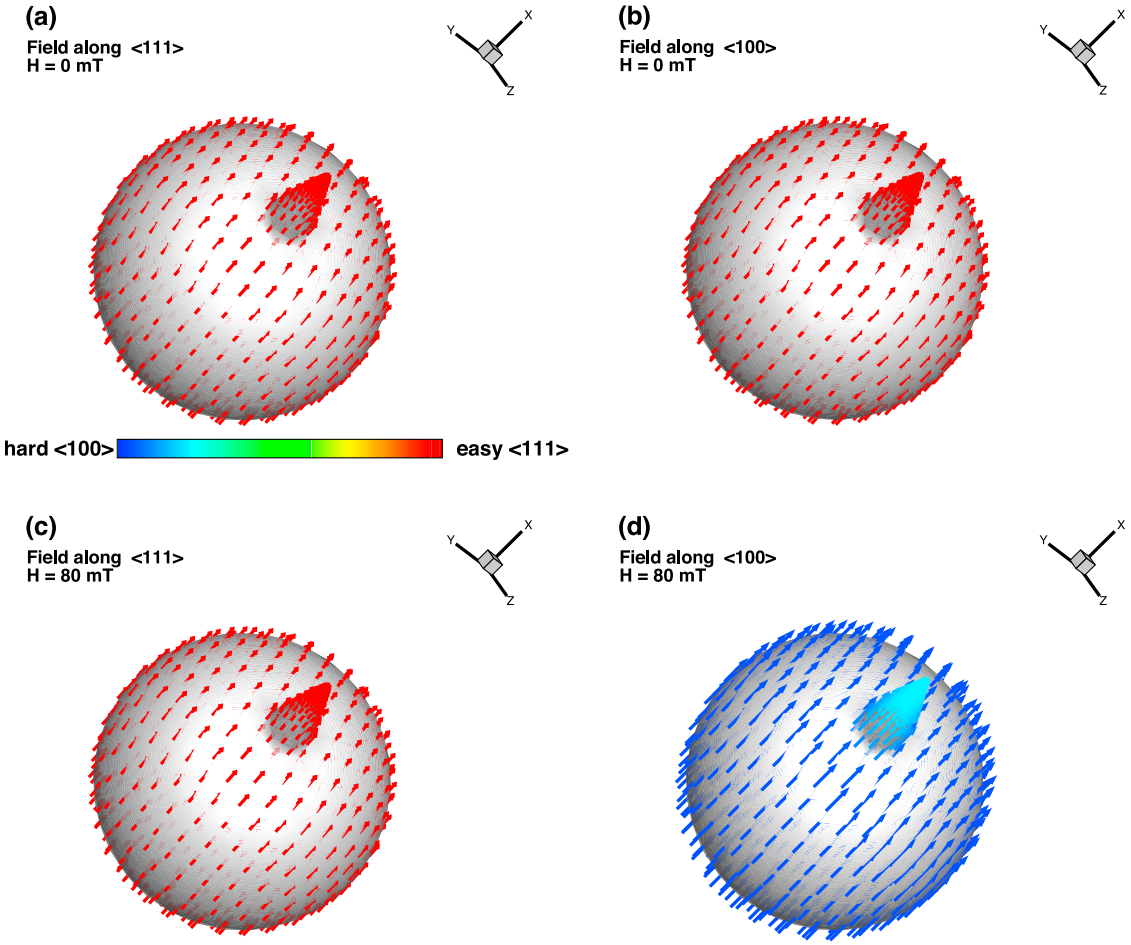

Figure 3. Micromagnetic structure of a 30 nm grain having a single large bump (R = 0.9) lying along the [111] (easy) axis. (a and b) H = 0 (Remanence); (c and d) H = 80 mT (Saturation). The field direction is indicated in each panel, and the resulting magnetization directions are colored according to the color bar in Figure 3a.

place with increases (decreases) when the bump lies along the easy (hard) axis for the 30 nm and 120 nm grains, with the opposite pattern occurring for the 90 nm grain. For the 30 nm SD grain, a large bump (R $\geq$ 0.7) along the hard ⟨100⟩ axis leads to micromagnetic structures that are increasingly unfavorable and are thus more easily demagnetized (H_c drops to 9 mT). The corollary holds for the easy ⟨111⟩ axis where the bump creates a more stable configuration with correspondingly higher coercivity (H_c = 18 mT). The situation is similar for the 120 nm PSD grain, except that it is the alignment of the vortex core that is now important. The micromagnetic calculations for the smooth grain show that the vortex core lies along the easy ⟨111⟩ axis (Figure 5a). A bump along this direction further favors this configuration and makes it even harder to demagnetize (H_c = 15 mT when R = 0.9), whereas a ⟨100⟩ bump has a weak effect in the opposite sense (H_c = 5 mT when R = 0.9). For the smooth 90 nm grain the micromagnetic solutions lead to a vortex core aligned along the hard ⟨100⟩ axis (Figure 5b). Addition of a bump in this direction stabilizes the configuration through magnetostatic and exchange coupling and consequently leads to increased coercivity, whereas bumps (of any size) in the easy ⟨111⟩ direction have virtually no effect on the already low coercivity.

3.2. Platonic Polyhedra

[12] As above, coercivities for all the models were obtained by averaging the values determined for fields along ⟨100⟩, ⟨110⟩ and ⟨111⟩, and the results shown in Figure 6. The addition of surface roughness to the 30 and 90 nm spheres has very little effect on coercivity. For the 120 nm grains, however, they give rise to a general increase as the bumps get larger with all three geometries

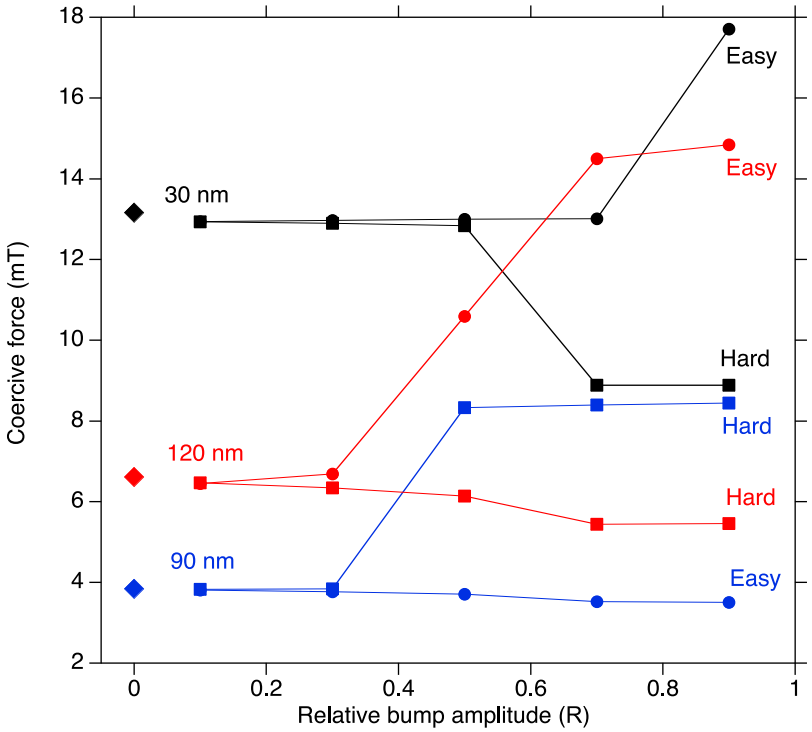

Figure 4. Coercive force (H_c) as a function of grain size, relative bump amplitude (R), and bump orientation (dots = easy ⟨111⟩ axis, squares = hard ⟨100⟩ axis). Diamonds are corresponding values for the smooth spheres [*Williams et al.* 2010].

closely agreeing for the smallest bumps (R = 0.1, $H_c \approx 6.5$ mT), and for the largest bumps (R = 0.9, $H_c \approx 11$ mT). The 120 nm tetrahedral model yields a smooth curve, but the other geometries show significant variations (particularly for the icosahedral geometry at R = 0.3 and the dodecahedral geometry at R = 0.7). For the icosahedral case this was checked by repeating the micro-

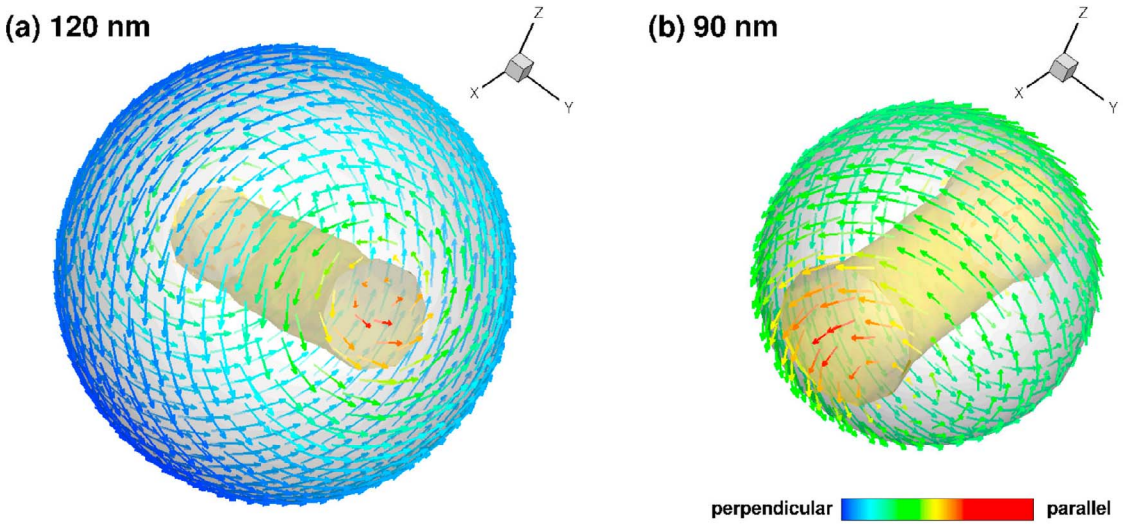

Figure 5. The remanence structure for the (a) 120 nm and (b) 90 nm smooth spheres. Both models have the same color coding and crystallographic orientation. Translucent 'cores' have been drawn for illustrative purposes. They are surfaces containing all moments lying within 22.5° of ⟨111⟩ for Figure 5a and ⟨100⟩ for Figure 5b. The overall geometry of the vortex cores is more clearly seen in Animation S3.

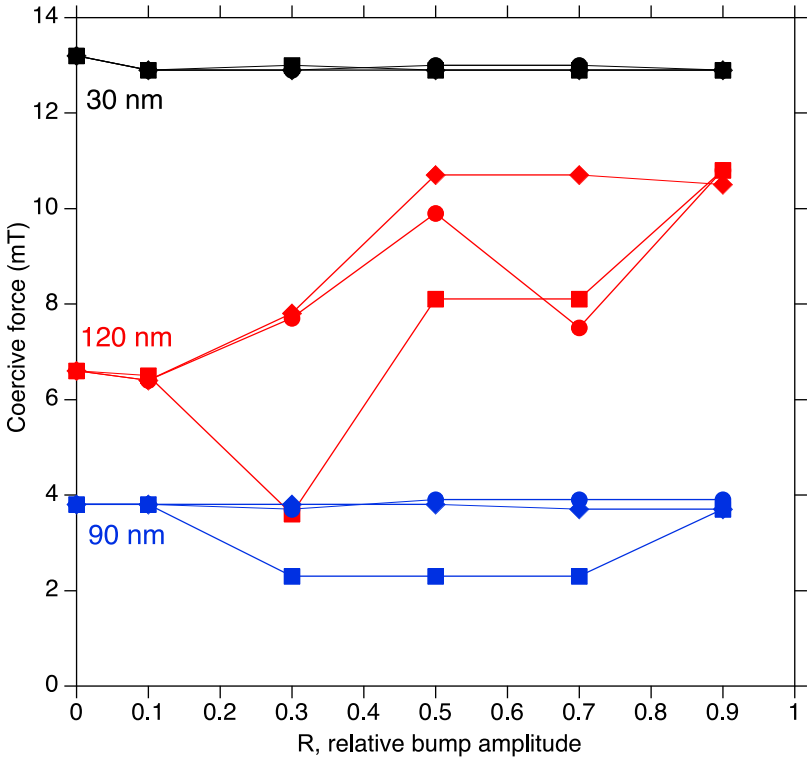

Figure 6. Coercivity (H_c) as a function of grain size, bump amplitude (R), and polyhedron geometry (diamond = tetrahedron, square = icosahedron, circle = dodecahedron). The values for smooth spheres (R = 0) are taken from *Williams et al.* [2010].

magnetic calculations at much higher resolution, but the same outlying low coercivity was found. Our experience with large numbers of models leads us to the conclusion that such variability is real and depends on the particular locations of the bumps relative to the crystal axes. This point becomes clear in what follows.

[13] To illustrate the micromagnetic structures behind the observed hardening trend, it is necessary to be selective since our entire computational scheme generates thousands of individual snapshots (33 field steps, 3 polyhedra, 5 bump amplitudes, 3 grain sizes, 3 field directions). We choose the tetrahedral case for R = 0.1 and R = 0.9, at a

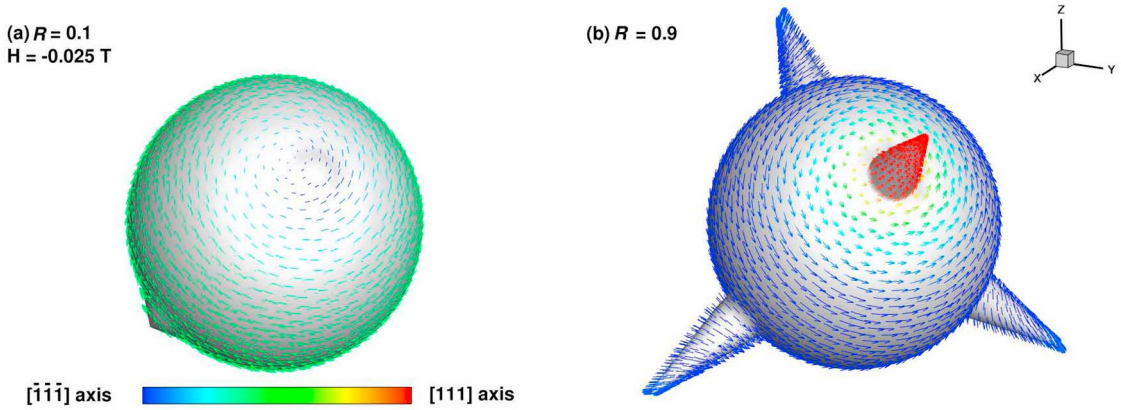

Figure 7. Micromagnetic structures for 120 nm tetrahedral geometry with bump amplitudes of (a) 0.1 and (b) 0.9. In both cases the field is −25 mT along the easy axis. The full dynamic behavior during field cycling can be seen in Animation S4.

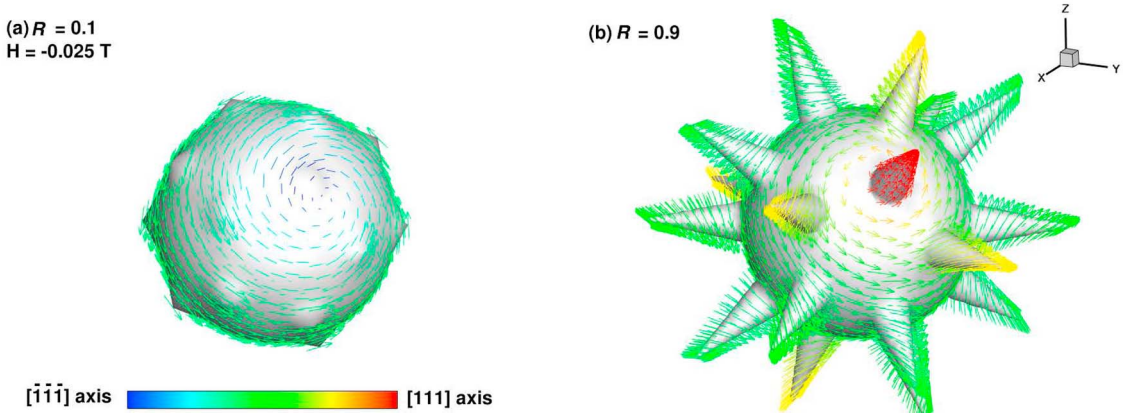

Figure 8. Micromagnetic structures for 120 nm dodecahedral geometry with bump amplitudes of (a) 0.1 and (b) 0.9. In both cases the field is −25 mT along the easy axis. The full dynamic behavior during field cycling can be seen in Animation S5.

particularly instructive field step (−25 mT) along the easy direction (Figure 7). This step is chosen because it clearly shows the effect of surface topography. For R = 0.9 the bump that lies closest to the applied field direction remains saturated in the forward direction and is directly connected to an underlying vortex. For the smaller bump (R = 0.1) the overall micromagnetic structure is essentially the same, but the bump has already switched to negative values. The full dynamic behavior of the magnetization during field cycling is shown in the Animation S4.

[14] Figure 8 parallels the situation depicted in Figure 7, but this time for the dodecahedral geometry. Once again, the effect of the surface topography is clearly seen. Depending on their exact location, bumps can act as pinning centers

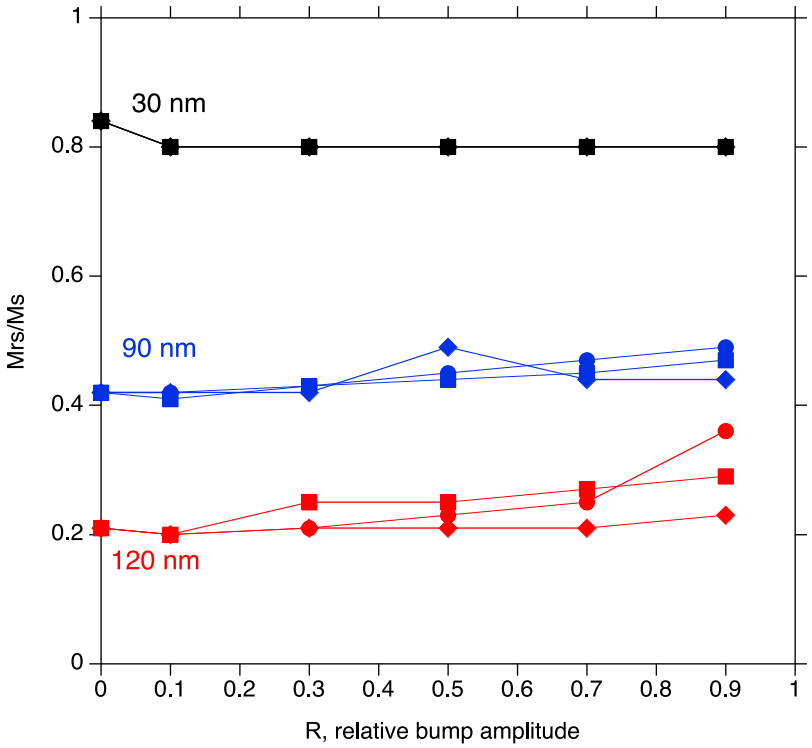

Figure 9. M_{rs}/M_s as a function of grain size, bump amplitude (R), and polyhedron geometry (diamond = tetrahedron, square = icosahedron, circle = dodecahedron).

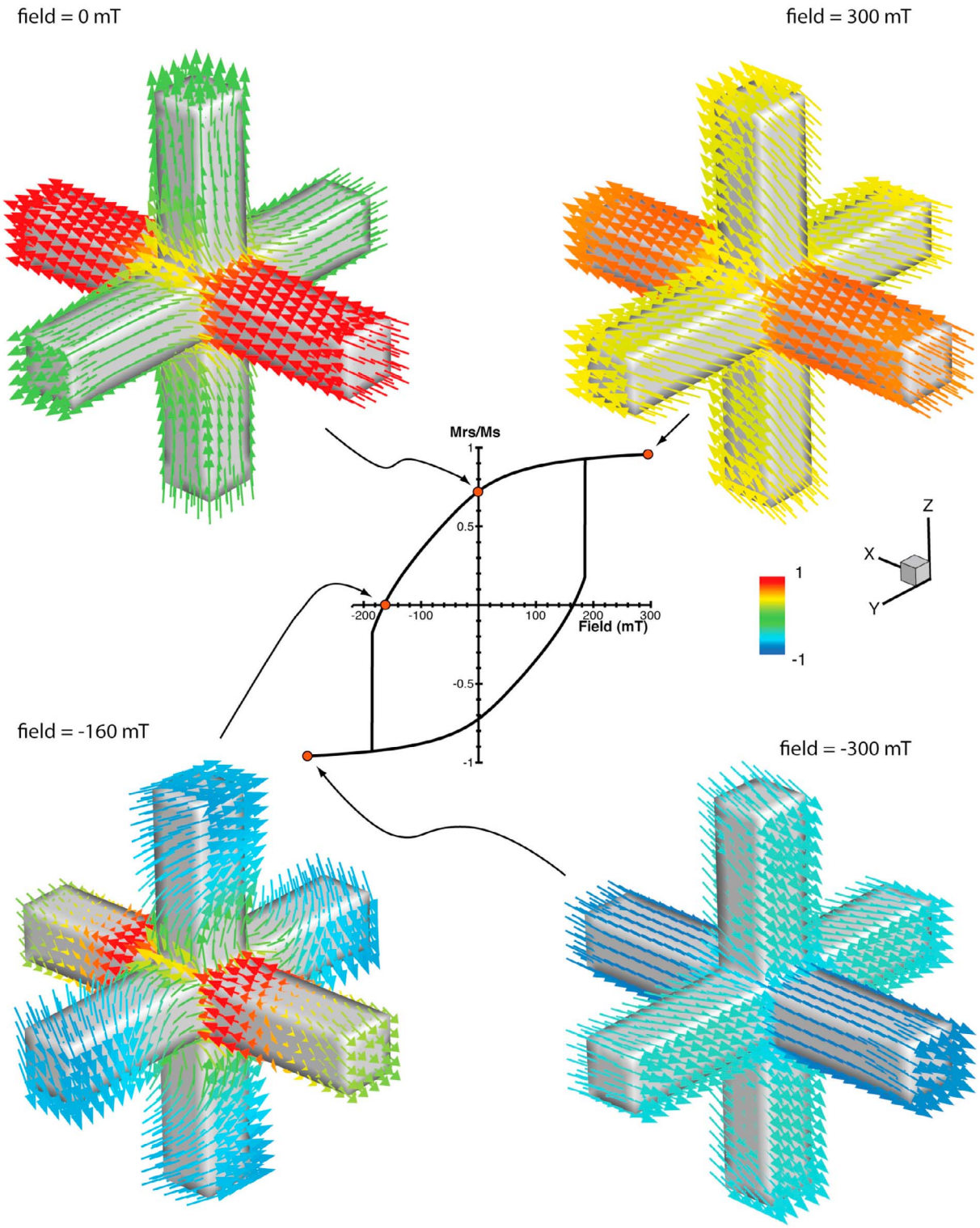

Figure 10. Computed hysteresis loop, and representative micromagnetic structures, for the triple-parallelepiped model discussed in the text. The structure consists of three intersecting prisms of size 140 nm × 20 nm × 20 nm. The applied field was varied in 0.5 mT steps. The hysteresis loop and coloring are for alignment in the *x* axis. The full dynamic behavior during field cycling can be seen in Animation S6.

and thereby increase the overall coercivity of the grain. This situation is somewhat different from the idea that surface irregularities cause changes in the local demagnetizing field and thus provide 'weak points' that can nucleate domain switching during hysteresis. Rather, our results indicate that the bumps of the scale we have modeled interact with the magnetocrystalline anisotropy and domain structure. Where the bumps align with the direction of the grain's magnetization they increase stability, and when they are situated at large angular separation from the underlying magnetization direction, the stability and coercivity of the grain is reduced.

[15] M_{rs}/M_s ratios for all the models are summarized in Figure 9, and again, there is a simple size-dependent pattern for the smooth spheres. As expected, M_{rs}/M_s is highest for the single-domain (30 nm) grains, and progressively decreases for the 90 and 120 nm grains. The bumps have virtually no effect for the SD grains, but very slight increases are seen for the 90 and 120 nm grains.

3.3. Orthogonal Parallelepiped Model

[16] The central purpose of the work described in this paper was to assess the magnetic behavior of magnetite grains having irregular surfaces in a manner that avoids unwanted shape anisotropy creeping in, as it did in our earlier work [*Williams et al.*, 2010]. Nevertheless, it is worthwhile to seek confirmation of the importance of shape anisotropy by considering grain morphologies that predict very high coercive forces. In particular, we are interested here in the "complicated shape" model discussed by *Tauxe et al.* [2002], which yielded coercivities beyond 100 mT. Most micromagnetic models predict much lower values, although classical theory does allow such values for elongated SD particles [*Stoner and Wohlfarth*, 1948] and real examples have been reported [*Hu et al.*, 2009]. The *Tauxe et al.* [2002] model consists of three mutually orthogonal intersecting parallelepipeds rather like the "dendrite" model we studied in our earlier paper [*Williams et al.*, 2010]. For the triple-parallelepiped model investigated here (each rod has dimensions of 140 × 20 × 20 nm), we generated a smooth hysteresis loop (Figure 10), which exhibited a coherent evolution of micromagnetic structure (available in Animation S6). The most important result is the confirmation of very high coercivities, H_c = 165 mT. This exceeds the value reported by *Tauxe et al.* [2002], and is far in excess of any of our Platonic polyhedron models. For M_{rs}/M_s we obtain 0.72, which is comparable to the ~0.69 reported by *Tauxe et al.* [2002]. For comparison, from analytical theory the coercivity for an elongated particle is given as $H_C = \mu_0 (N_a - N_b) M_S$ where N_a and N_b are the demagnetizing factors along the long and short axis of the particle respectively. The values for the demagnetizing factors can be calculated analytically for rectangular parallelepipeds [*Aharoni*, 1998] and for a single prism with the same aspect ratio of one of the limbs of the particle described above, yields a coercivity of 243 mT. This suggests that the skeletal structure helps to nucleate curling structures, reducing the coercivity.

4. Conclusions

[17] A micromagnetic analysis of magnetite grains having surface roughness, but no overall shape anisotropy, leads to the conclusion that irregular morphologies do not enhance the coercivity of small grains lying in the SD field or near the SD/PSD boundary. For grains within the PSD field, however, surface irregularities can almost double the coercivity and hence lead to increased paleomagnetic stability. The origin of the increased stability appears to be the alignment of the bumps with the equilibrium direction of the grain's magnetization for any particular applied field. The very high coercivities found in some rocks cannot be attained by surface roughness models and can only be explained by shape anisotropy. This is confirmed by our high-resolution micromagnetic computations for a "skeletal" grain consisting of three mutually perpendicular parallelepipeds, which exhibits a coercive force well in excess of 100 mT.

Acknowledgments

[18] The work described in this paper was initiated during the tenure of a Leverhulme Visiting Professorship to M.E.E. Ongoing financial support was also provided by the Natural Sciences and Engineering Research Council of Canada, the Natural Environment Research Council of the UK, and the Royal Society of London.

References

Aharoni, A. (1998), Demagnetizing factors for rectangular ferromagnetic prisms, *J. Appl. Phys.*, *83*, 3432–3434, doi:10.1063/1.367113.

Enkin, R. J., and W. Williams (1994), Three-dimensional micromagnetic analysis of stability in fine magnetic grains, *J. Geophys. Res.*, *99*, 611–618, doi:10.1029/93JB02637.

Hu, M., J.-S. Jiang, and X. Li (2009), Surfactant-assisted hydrothermal synthesis of dendritic magnetite microcrystals, *Cryst. Growth Des.*, *9*, 820–824, doi:10.1021/cg8003933.

Rave, W., K. Ramstöck, and A. Hubert (1998), Corners and nucleation in micromagnetics, *J. Magn. Magn. Mater.*, *183*, 329–333, doi:10.1016/S0304-8853(97)01086-X.

Stacey, F. D. (1961), Theory of the magnetic properties of igneous rocks in alternating fields, *Philos. Mag.*, *6*, 1241–1260, doi:10.1080/14786436108243374.

Stoner, E. C., and E. P. Wohlfarth (1948), A mechanism of magnetic hysteresis in heterogeneous alloys, *Philos. Trans. R. Soc. London A*, *240*, 599–642, doi:10.1098/rsta.1948.0007.

Suess, D., V. Tsiantos, T. Schrefl, J. Fidler, W. Scholz, H. Forster, R. Dittrich, and J. J. Miles (2002), Time resolved micromagnetics using a preconditioned time integration method, *J. Magn. Magn. Mater.*, *248*, 298–311, doi:10.1016/S0304-8853(02)00341-4.

Tauxe, L., H. N. Bertram, and C. Seberino (2002), Physical interpretation of hysteresis loops: Micromagnetic modeling of fine particle magnetite, *Geochem. Geophys. Geosyst.*, *3*(10), 1055, doi:10.1029/2001GC000241.

Williams, W., A. R. Muxworthy, and G. A. Paterson (2006), Configurational anisotropy in single-domain and pseudosingle-domain grains of magnetite, *J. Geophys. Res.*, *111*, B12S13, doi:10.1029/2006JB004556.

Williams, W., M. E. Evans, and D. Krása (2010), Micromagnetics of paleomagnetically significant mineral grains with complex morphology, *Geochem. Geophys. Geosyst.*, *11*, Q02Z14, doi:10.1029/2009GC002828.